Synthesis and Li-Ion Insertion Properties of Highly Crystalline Mesoporous Rutile TiO_2

Donghai Wang,[†] Daiwon Choi,[†] Zhenguo Yang,[†] Vilayanur V. Viswanathan,[†] Zimin Nie,[†] Chongmin Wang,[†] Yujiang Song,[‡] Ji-Guang Zhang,[†] and Jun Liu*,[†]

Pacific Northwest National Laboratory, Richland, Washington, 99352, and Sandia National Laboratory, Albuquerque, New Mexico, 87185

Received January 25, 2008. Revised Manuscript Received February 12, 2008

Mesoporous TiO_2 has attracted great attention as a promising Li insertion electrode material with improved cycling life, rate capability, and high power density. Up to date, mesoporous anatase TiO_2 has been investigated for Li insertion. Recent studies have shown that nanosized rutile could be an excellent candidate for anode materials for higher Li insertion capacity and improved stability. However, synthesis of highly crystalline mesoporous rutile has met with limited success so far. There has been no report on Li insertion of mesoporous rutile TiO_2. In this paper, we report a new low-temperature solution growth of TiO_2 nanocrystals within an anionic surfactant matrix to produce highly crystalline mesoporous rutile and investigate Li insertion properties of the mesoporous crystalline rutile. X-ray diffraction (XRD) patterns and N_2 sorption isotherms reveal that mesoporous structure in the highly crystalline mesoporous TiO_2 directly results from the anionic surfactant templating effects with high surface area (245−300 m^2/g) and tunable mesopore diameter ranging from 2.2 to 3.8 nm after calcination. Transmission electron microscopy (TEM) measurements show that framework of the highly crystalline mesoporous TiO_2 are composed of aligned rutile nanorod building blocks grown along [001] direction. The new mesoporous crystalline rutile can accommodate more than 0.7 Li ($Li_{0.7}TiO_2$, 235 mA h g^{-1}) during the first discharge at a *C*/5 rate between 1 and 3 V versus Li^+/Li, with a reversible capacity of 0.55 Li ($Li_{0.55}TiO_2$, 185 mA h g^{-1}). The mesoporous crystalline rutile shows excellent capacity retention with less than 10% capacity loss after more than 100 cycles. XRD and TEM characterization on the electrochemically lithiated sample show that the rutile nanorods were transformed into cubic rocksalt $LiTiO_2$ nanorods, but the mesostructures remained stable after the phase transformation and cycling. Furthermore, the crystalline mesoporous rutile may also have good potential for other applications such as stable catalyst supports.

Introduction

With great success in portable electronics, Li-ion batteries are considered the most promising energy storage technologies for electric vehicles and renewable energy systems operated on intermittent sources such as wind and solar. For the emerging applications, however, fundamental improvements are needed with regard to power, safety, cycle life, and cost. For example, graphite widely used as anodes in commercial Li-ion batteries has an operating voltage close to Li electroplating and forms a solid electrolyte interface (SEI layer), raising concerns over safety and loss of capacity.[1–3] A potential alternative anode TiO_2 is an abundant, low-cost, and environmentally benign material that has a redox potential of 1.5−1.8 V vs Li^+/Li redox couple, and thereby is inherently safe by avoiding Li electroplating. In addition, Li-ion insertion/extraction in TiO_2-based structures is accompanied by negligible lattice changes, leading to enhanced structural stability and longer cycle life. One drawback, however, is that the poor lithium ionic and electronic conductivity of bulk TiO_2 polymorphs limited their charge/discharge rate.

To overcome the issue, TiO_2 polymorphs have been prepared as nanosized or nanoporous particles to reduce the Li-diffusion length in the solid phase and improve their cycling life due to minimized strain during Li ion insertion/extraction.[4–6] For example, nanosized anatase,[7–10] rutile,[11–14] spinel $Li_4Ti_5O_{12}$[15,16] and nanostructured anatase or titanate nano-

* Corresponding author. E-mail: jun.liu@pnl.gov.
[†] Pacific Northwest National Laboratory.
[‡] Sandia National Laboratory.

(1) Croce, F.; Appetecchi, G. B.; Persi, L.; Scrosati, B. *Nature* **1998**, *394*, 456.
(2) Tarascon, J. M.; Armand, M. *Nature* **2001**, *414*, 359.
(3) Nelson, R. F. *J. Power Sources* **2000**, *91*, 2.
(4) Maier, J. *Nat. Mater.* **2005**, *4*, 805.
(5) Wang, Y.; Cao, G. Z. *Chem. Mater.* **2006**, *18*, 2787.
(6) Sides, C. R.; Li, N. C.; Patrissi, C. J.; Scrosati, B.; Martin, C. R. *MRS Bull.* **2002**, *27*, 604.
(7) Jiang, C. H.; Wei, M. D.; Qi, Z. M.; Kudo, T.; Honma, I.; Zhou, H. S. *J. Power Sources* **2007**, *166*, 239.
(8) Kavan, L.; Graetzel, M.; Rathousky, J.; Zukal, A. *J. Electrochem. Soc.* **1996**, *143*, 394.
(9) Liu, Z. L.; Hong, L.; Guo, B. *J. Power Sources* **2005**, *143*, 231.
(10) Exnar, I.; Kavan, L.; Huang, S. Y.; Graetzel, M. *J. Power Sources* **1997**, *68*, 720.
(11) Hu, Y. S.; Kienle, L.; Guo, Y. G.; Maier, J. *Adv. Mater.* **2006**, *18*, 1421.
(12) Baudrin, E.; Cassaignon, S.; Koesch, M.; Jolivet, J. P.; Dupont, L.; Tarascon, J. M. *Electrochem. Commun.* **2007**, *9*, 337.
(13) Jiang, C. H.; Honma, I.; Kudo, T.; Zhou, H. S. *Electrochem. Solid-State Lett.* **2007**, *10*, A127.
(14) Reddy, M. A.; Kishore, M. S.; Pralong, V.; Caignaert, V.; Varadaraju, U. V.; Raveau, B. *Electrochem. Commun.* **2006**, *8*, 1299.
(15) Guerfi, A.; Sevigny, S.; Lagace, M.; Hovington, P.; Kinoshita, K.; Zaghib, K. *J. Power Sources* **2003**, *119*, 88.

10.1021/cm8002589 CCC: $40.75
Published on Web 05/03/2008

tube[17–19] as well as TiO_2-B nanowire[20–22] have been reported showing a higher capacity and much improved capacity retention and rate capability in comparison with that of bulk materials. Nanoporous TiO_2 may also provide the additional advantages: (1) large surface area increases the electrode/electrolyte contact area, which decreases the current density per unit surface area, leading to higher charge/discharge rate; (2) mesopore structure provides a short path distance for Li^+ transport, permitting battery to use materials with low ionic conductivity. Actually, it has been demonstrated that mesoporous anatase TiO_2 with controlled pore structure is an effective Li-ion insertion electrode material with capacity close to or exceeding theoretical value of lithiated anatase ($Li_{0.5}TiO_2$,168 mA h g^{-1}), although there is still capacity loss after cycling.[23–27] The porous structure can also facilitate the incorporation of secondary conducting components (e.g., carbon nanotube,[28] SnO_2/CuO,[29] RuO_2[30]) within the mesoporous structure to enhance the electron conductivity of the mesoporous electrode and thus further improve high-rate charge–discharge performance. To date, Li insertion studies in mesoporous TiO_2 are mainly focused on anatase phase. There is no report on Li insertion properties of mesoporous rutile, to the best of our knowledge. Recently, it has been reported that nanosized rutile TiO_2 can reversibly accommodate 0.5 Li ($Li_{0.5}TiO_2$), which is comparable to that of anatase,[11,12] even though bulk rutile can only accommodate a negligible amount of Li (<0.1 Li per TiO_2 unit) at room temperature. Jiang et al. reported that Li insertion in 15 nm sized rutile TiO_2 can be reversibly cycled up to $Li_{0.6-0.7}TiO_2$ with good capacity rentention.[13] These findings on Li insertion in nanocrystalline rutile provide new incentives to synthesize highly crystalline mesoporous rutile TiO_2 with high surface area and investigate their electrode performance.

Mesoporous TiO_2 is normally synthesized using surfactant templating routes at low temperature (<200 °C) to produce the anatase phase.[31] Converting anatase nanocrystals to rutile at high temperature would however cause structural collapse. A few groups explored surfactant templated synthesis of mesoporous rutile made of aggregated amorphous or nanocrystalline particles.[32–34] However, synthesis of stable, highly crystalline mesoporous rutile remains challenging. Alternatively, hydrothermal synthesis[33,35] or an ionic liquid[36,37] has been used to produce aggregates made of crystalline, aligned rutile nanorods in which some mesopores could be observed.

The objective of this study is first to develop a surfactant templated route to synthesize highly crystalline mesoporous rutile and then investigate the Li-ion insertion capacity, the structural transformation, and stability of such new materials during long charge–discharge cycles. To control the crystallization kinetics and the degree of cross-linking, we adapted a strategy for rutile synthesis in which the solubility and precipitation were controlled by hydrolysis and oxidation of titanium trichloride.[38,39] Also, many studies found that the anions such as sulfate, whether present in the solution or derived from the precursor, have high affinity for chelating TiO_2.[39–42] On the basis of these results, we chose anionic sulfate or sulfonic surfactants so that the strong binding with TiO_2 would keep the surfactant in the structure when the crystallization occurs. The processing parameters were optimized to obtain the highly crystalline mesoporous rutile TiO_2 nanostructures, designated as MCTs. Li-ion insertion properties on the mesoporous crystalline rutile TiO_2 were investigated showing high capacity with excellent capacity retention. This paper also reports direct observation of the phase transition in MCTs from crystalline rutile to cubic rocksalt $LiTiO_2$ after electrochemical Li insertion/extraction cycles, which is consistent with the reported structure change from rutile to the cubic $LiTiO_2$ phase in previous studies based on ex situ formed sample via mechanical grinding.[12] TEM analysis on nanorod morphology, crystallographic alignment and mesostructure–stability is also investigated after prolonged cycling of Li insertion/extraction. The highly crystalline mesoporous rutile with high surface area is another promising addition to Li-insertion TiO_2 electrodes, which may provide a new materials platform for synthesis of composite electrode and fabrication of three-dimensional battery architecture.

Experimental Section

Materials. Titanium trichloride, sodium n-decyl-1-sulfonate, sodium dodecyl sulfate, sodium 1-hexadecanesulfonate, hydrogen peroxide (30 wt % aqueous solution), hydrochloride acid, dimethyl carbonate (99+%, Anhydrous), and N-methylpyrroli-

(16) Kavan, L.; Graetzel, M. *Electrochem. Solid-State Lett.* **2002**, *5*, A39.
(17) Li, J. R.; Tang, Z. L.; Zhang, Z. T. *Electrochem. Commun.* **2005**, *7*, 62.
(18) Zhou, Y. K.; Cao, L.; Zhang, F. B.; He, B. L.; Li, H. L. *J. Electrochem. Soc.* **2003**, *150*, A1246.
(19) Gao, X. P.; Lan, Y.; Zhu, H. Y.; Liu, J. W.; Ge, Y. P.; Wu, F.; Song, D. Y. *Electrochem. Solid-State Lett.* **2005**, *8*, A26.
(20) Armstrong, A. R.; Armstrong, G.; Canales, J.; Garcia, R.; Bruce, P. G. *Adv. Mater.* **2005**, *17*, 862.
(21) Armstrong, A. R.; Armstrong, G.; Canales, J.; Bruce, P. G. *Angew. Chem., Int. Ed.* **2004**, *43*, 2286.
(22) Zukalova, M.; Kalbac, M.; Kavan, L.; Exnar, I.; Gratzel, M. *Chem. Mater.* **2005**, *17*, 1248.
(23) Attia, A.; Zukalova, M.; Rathousky, J.; Zukal, A.; Kavan, L. *J. Solid State Electrochem.* **2005**, *9*, 138.
(24) Moriguchi, I.; Hidaka, R.; Yamada, H.; Kudo, T. *Solid State Ionics* **2005**, *176*, 2361.
(25) Guo, Y. G.; Hu, Y. S.; Maier, J. *Chem. Commun.* **2006**, 2783.
(26) Kavan, L.; Rathousky, J.; Graetzel, M.; Shklover, V.; Zukal, A. *J. Phys. Chem. B* **2000**, *104*, 12012.
(27) Kavan, L.; Attia, A.; Lenzmann, F.; Elder, S. H.; Gratzel, M. *J. Electrochem. Soc.* **2000**, *147*, 2897.
(28) Moriguchi, I.; Hidaka, R.; Yamada, H.; Kudo, T.; Murakami, H.; Nakashima, N. *Adv. Mater.* **2006**, *18*, 69.
(29) Zhou, H. S.; Li, D. L.; Hibino, M.; Honma, I. *Angewandte Chemie-International Edition* **2005**, *44*, 797.
(30) Guo, Y. G.; Hu, Y. S.; Sigle, W.; Maier, J. *Adv. Mater.* **2007**, *19*, 2087.
(31) Antonelli, D. M.; Ying, J. Y. *Angew. Chem., Int. Ed.* **1995**, *34*, 2014.
(32) Samuel, V.; Muthukumar, P.; Gaikwad, S. P.; Dhage, S. R.; Ravi, V. *Mater. Lett.* **2004**, *58*, 2514.
(33) Li, Y. Z.; Lee, N. H.; Lee, E. G.; Song, J. S.; Kim, S. J. *Chem. Phys. Lett.* **2004**, *389*, 124.
(34) Luo, H. M.; Wang, C.; Yan, Y. S. *Chem. Mater.* **2003**, *15*, 3841.
(35) Li, J. G.; Ishigaki, T.; Sun, X. D. *J. Phys. Chem. C* **2007**, *111*, 4969.
(36) Yu, N. Y.; Gong, L. M.; Song, H. J.; Liu, Y.; Yin, D. H. *J. Solid State Chem.* **2007**, *180*, 799.
(37) Kaper, H.; Endres, F.; Djerdj, I.; Antonietti, M.; Smarsly, B. M.; Maier, J.; Hu, Y. S. *Small* **2007**, *3*, 1753.
(38) Hosono, E.; Fujihara, S.; Kakiuchi, K.; Imai, H. *J. Am. Chem. Soc.* **2004**, *126*, 7790.
(39) Wang, D. H.; Liu, J.; Huo, Q. S.; Nie, Z. M.; Lu, W. G.; Williford, R. E.; Jiang, Y. B. *J. Am. Chem. Soc.* **2006**, *128*, 13670.
(40) Baskaran, S.; Song, L.; Liu, J.; Chen, Y. L.; Graff, G. L. *J. Am. Ceram. Soc.* **1998**, *81*, 401.
(41) Bunker, B. C.; Rieke, P. C.; Tarasevich, B. J.; Campbell, A. A.; Fryxell, G. E.; Graff, G. L.; Song, L.; Liu, J.; Virden, J. W.; McVay, G. L. *Science* **1994**, *264*, 48.
(42) Li, Y. Z.; Lee, N. H.; Hwang, D. S.; Song, J. S.; Lee, E. G.; Kim, S. J. *Langmuir* **2004**, *20*, 10838.

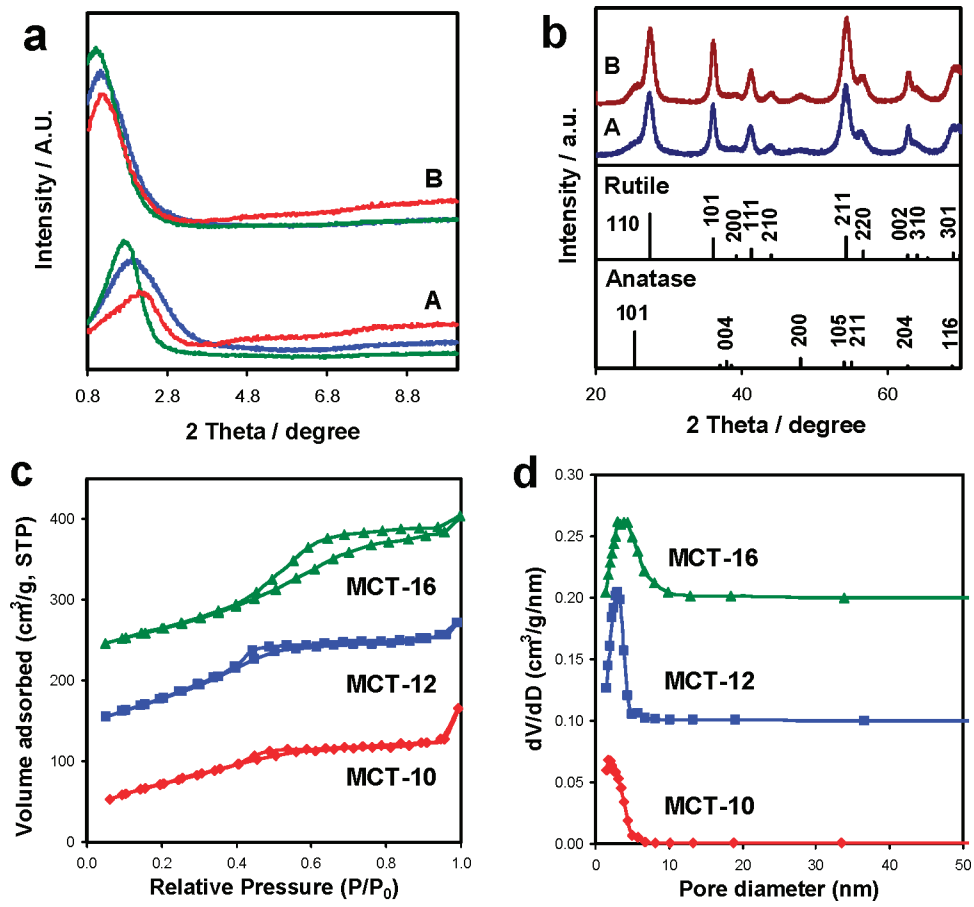

Figure 1. (a) Low-angle XRD patterns of MCT-10 (red), MCT-12 (blue), and MCT-16 (green) (A) before and (B) after calcination. (b) High-angle XRD patterns of (A) as-synthesized and (B) calcined MCT-12. Standard reflection peaks of rutile (JCPDS 21-1276) and anatase (JCPDS No. 21-1272) were shown as vertical bars. (c) Nitrogen sorption isotherms of MCTs. The isotherms for MCT-12 and MCT-16 were offset vertically by 100 and 200 cm^3/g, respectively. (d) BJH pore size distribution of MCTs from adsorption data. The distribution of MCT-12 and MCT-16 were offset vertically by 0.1 and 0.2 $cm^3\ g^{-1}\ nm^{-1}$, respectively.

done were purchased from Sigma-Aldrich. Li foil and poly(vinylidene fluoride) were purchased from Alfa Aesar. Super P was purchased from TIMCAL Graphite & Carbon. Electrolyte consisting of 1 M $LiPF_6$ in ethyl carbonate/dimethyl carbonate (2:1 in volume) was obtained from EM Industries (Merck KGaA, Darmstadt, Germany)

Synthesis and Characterization of MCTs. In a typical synthesis of MCT-10 or MCT-12, a 7.33 mL aliquot of 20 mg/mL sodium n-decyl-1-sulfonate solution (0.6 mmol) or a 1.2 mL aliquot of 0.5 M sodium dodecyl sulfate solution (0.6 mmol) was added into a 10 mL solution of 0.12 M $TiCl_3$ (1.2 mmol) under vigorous stirring. For the synthesis of MCT-16, a 3.94 mL aliquot of 20 mg/mL sodium 1-hexadecanesulfonate solution (0.24 mmol) at 60 °C was added into a 10 mL aliquot of 0.12 M $TiCl_3$ (1.2 mmol) in a 1.0 M HCl solution under vigorous stirring.

To these corresponding mixtures, a 0.8 mL aliquot of 1% hydrogen peroxide solution (0.24 mmol) was added dropwise under vigorous stirring. Then, 35 mL deionized water were added under vigorous stirring. The final mixture was further stirred in a polypropylene flask for 15 h at 60 °C to obtain a white mixture. The precipitated product was collected by centrifuge at 10 000 rpm for 10 min followed by washing with deionized water and ethanol. The product was then dried in a vacuum oven at 60 °C overnight and subsequently calcined in air at 400 °C for 2 h.

XRD patterns in $\theta-2\theta$ scan mode were obtained using a Philips Xpert X-ray diffractometer using Cu Kα radiation at λ1.54 Å. FESEM investigation was performed using a Hitachi S5200 operated at 25.0 kV. TEM images were collected on a JEOL JSM-2010 TEM microscope operated at 200 kV. Nitrogen adsorption data were collected using Quantachrome autosorb automated gas sorption systems.

Electrochemical Characterization. Electrochemical experiments were carried out using two-electrode coin cells (Type 2335). Li foil was used as counter electrode. For preparation of the working electrode, a mixture of calcined mesoprous rutile, super P carbon black, and poly(vinylidene fluoride) (PVDF) binder were dispersed in N-methylpyrrolidone (NMP) solution in a weight ratio of 80:10:10, respectively. The slurry was then coated on an aluminum foil current collector and dried overnight in air. The electrolyte used was 1 M $LiPF_6$ in ethyl carbonate/dimethyl carbonate (EC/DMC) (2:1). The coin cells were assembled in an argon-filled glovebox. The electrochemical performance of the mesoporous TiO_2 was evaluated in an Arbin Battery Testing System at room temperature. The cells were tested between 3 and 1 V versus Li^+/Li at various rates (1*C* to *C*/10).

Results and Discussion

To study the effect of surfactant templating, we investigated anionic surfactants of different chain lengths. The samples generated with anionic surfactant $C_{10}H_{21}SO_3Na$, $C_{12}H_{25}SO_4Na$, and $C_{16}H_{33}SO_3Na$ are designated MCT-10, MCT-12, and MCT-16, respectively. The as-synthesized MCTs all show a broad low angle X-ray reflection peak with *d*-spacing in the range between 3.9 and 5.0 nm (Figure 1a), indicative of short-range mesoscale ordering. In addition, the

low-angle diffraction peaks consistently shift to a lower angle with increasing chain length of anionic surfactants, suggesting that the short-range mesoscale ordering is determined by the surfactant chain length. After calcination, the low-angle reflection peaks shift to high *d*-spacing values, which is characteristic of the short-range correlation between mesopores with a denser and thicker framework. For all the calcined MCTs, the diffraction peaks also shift systematically as a function of surfactant chain length. High-angle XRD patterns (Figure 1b) confirm that as-synthesized MCTs contain crystalline, rutile TiO_2 with a small amount of anatase TiO_2 (less than 5% anatase in the as-synthesized sample estimated from XRD results[43]). Enhanced rutile [002] and [211] reflection peaks are observed compared with rutile standard peak intensity in the XRD patterns of MCT-12, which may result from the preferred growth of nanocrystals along [001] direction. We have analyzed the composition of the samples after calcination using energy dispersive spectrometry (EDS) in the transmission electron microscopy mode and X-ray photoelectron spectroscopy (XPS) techniques. No significant amount of S was detected under EDS. Less than 3.5 atomic % S was detected using XPS. Because XPS is surface sensitive, this result suggests that a very small amount of S may be absorbed on the TiO_2 surface.

Results from nitrogen sorption measurement show type-IV isotherms with a rather narrow distribution of mesopore diameter (panels c and d in Figure 1). The adsorption data indicate Brunauer–Emmett–Teller (BET) surface areas of 266, 300, and 245 m^2/g for MCT-10, MCT-12, and MCT-16 after calcination, respectively. A hysteresis in N_2 adsorption isotherms of MCT-16 is usually characteristic of slitlike mesopores.[44] The pore size distributions calculated by Barrett-Joynes-Halenda (BJH) model using the adsorption branch show systematic increase of pore size, from 2.2, to 3.1, to 3.8 nm, in calcined MCT-10, MCT-12 to MCT-16, respectively. The pore diameters for MCT-10, MCT-12, and MCT-16 roughly agree with the micelle sizes expected from $C_{10}H_{21}SO_3Na$, $C_{12}H_{25}SO_4Na$, and $C_{16}H_{33}SO_3Na$ with chain lengths of 1.2, 1.4, and 1.9 nm, respectively. The pore volume is 0.256, 0.265, and 0.315 mL/g for MCT-10, MCT-12, and MCT-16, respectively. Therefore, both the diffraction and the nitrogen adsorption data suggest that surfactant template played an important role in determining the pore structure.

Images a and b in Figure 2 show typical transmission electron microscopy (TEM) images of as-synthesized MCTs. The composite aggregates are all made of well-defined, "periodic" straight rodlike features, closely resembling the mesostructure in periodic mesoporous silica. The rod-like features in MCT-10 (Figure 2a) are oriented radially from central region toward the edges of the particle, which are identical to the mesoporous silica spherulites made of rodlike micelles.[45] The surfactant with longer chain length produced more elongated aggregates in MCT-12 (Figure 2b) and MCT-16 (data not shown). Selected area electron diffraction (SAED) patterns (insets in Figure 2a) on a striped grain reveal crystalline rutile phase. The SAED patterns also show a pair of strong (110) reflections, indicating that the (110) planes of the rutile nanocrystals are locally preferably oriented. The dark-field image (inset in Figure 2b) shows a bright parallel rodlike feature, indicating that aligned elongated nanocrystals formed within the stripe patterned structures. The overall stripe-patterned mesostructures of the MCTs were well preserved after calcination. For instance, Figure 2c shows corresponding TEM images of calcined MCT-10 with features similar to that in Figure 2a. SAED patterns also show pairs of strong (110) reflections spots, indicating presence of oriented rutile nanocrystals. High-resolution scanning electron microscopy (SEM) further confirms calcined MCT-10 is indeed composed of interspaced rodlike nanocrystals (Figure 2d). Radial organization of uniform rodlike nanocrystals (3 nm in diameter) with roughly 2 nm spacing are revealed in region A of Figure 2d, whereas mesopores as well as cross-linking feature of the rodlike nanocrystals are shown from top view marked in region B. Here, some nanocrystals appear fused together, and the space between the rods can be observed as either cylindrical channels or slits. Similar parallel aggregated structures of rodlike nanocrystals and interspacing between the nanocrystals are also observed in calcined MCT-12 and MCT-16.

The morphology of the "rodlike" features in MCTs show some resemblance to those reported in the rutile aggregates.[33,35,36] However, the new MCT materials have unique properties that are not present in the rutile aggregates reported in the previous studies. First, the width at half-height position of the peak in pore size distribution (Figure 1d) is only about 2.5 nm for MCT-12 and 5 nm for MCT-16. In comparison, the MCTs have narrower pore size distributions than that of the reported mesoporous rutile aggregates.[32,36] In addition, the low-angle diffractions were not reported in the previous studies. More importantly, the MCT materials show systematic pore size change and good correlation of the pore sizes and the surfactant chain length. These results suggest that the MCTs have properties typical of mesoporous materials formed from a surfactant templated route.

Detailed TEM studies further confirmed that the rod-like nanocrystals in MCTs are aligned or grown along [001] directions. As shown in Figure 3a, only parallel, (110) lattice fringes were observed along the length of each rodlike nanocrystals identified by the spacing of adjacent lattice fringes equals to 0.32 nm, indicating that rutile nanocrystals were grown along the [001] directions. Viewed in a different zone axis, Figure 3b shows the cross lattice fringe of (101) planes with good alignment over the entire region identified by 0.26 nm spacing of adjacent lattice fringes, which also confirms [001]-oriented rutile rodlike nanocrystals along its length. Thus it can be concluded that the crystalline structures are well-aligned not only along the [001] growth orientation, but also crystallographically arranged in the transverse directions over a few ten nanometers in the as-synthesized MCT-12. Similarly, high-resolution TEM analysis on calcined MCT-12 (Figure 3c) found parallel rutile (110) lattice fringes along the length of rod-like nanocrystals indicating

(43) Zhang, H. Z.; Banfield, J. F. *J. Phys. Chem. B* **2000**, *104*, 3481.
(44) Sing, K. S. W.; Everett, D. H.; Haul, R. A. W.; Moscou, L.; Pierotti, R. A.; Rouquerol, J.; Siemieniewska, T. *Pure Appl. Chem.* **1985**, *57*, 603.
(45) Liu, J. K.; A, Y; Virden, J. W.; Bunker, B. C *J. Porous Mater.* **1996**, *2*, 201.

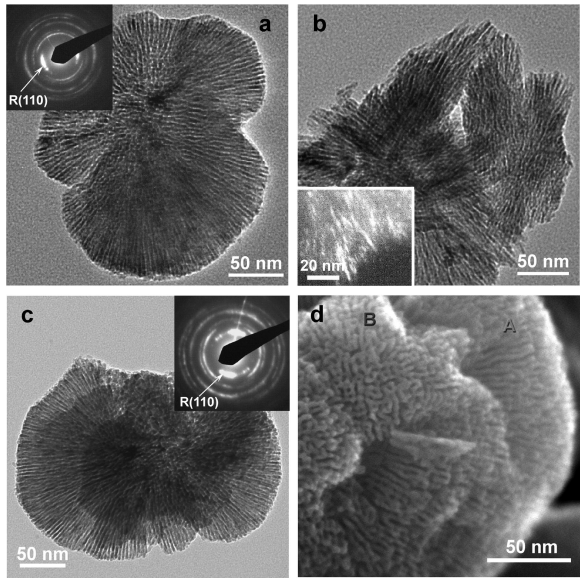

Figure 2. (a, b) TEM images of as-synthesized (a) MCT-10 and (b) MCT-12. Inset in (a) shows corresponding SAED patterns. Inset in (b) shows a dark-field TEM image. (c) TEM image of calcined MCT-10. Inset shows corresponding SAED patterns. (d) High-resolution SEM image of calcined MCT-10. Regions A and B are marked representing the side view and top view, respectively, of the stripe-patterned mesostructure composed of rodlike nanocrystals.

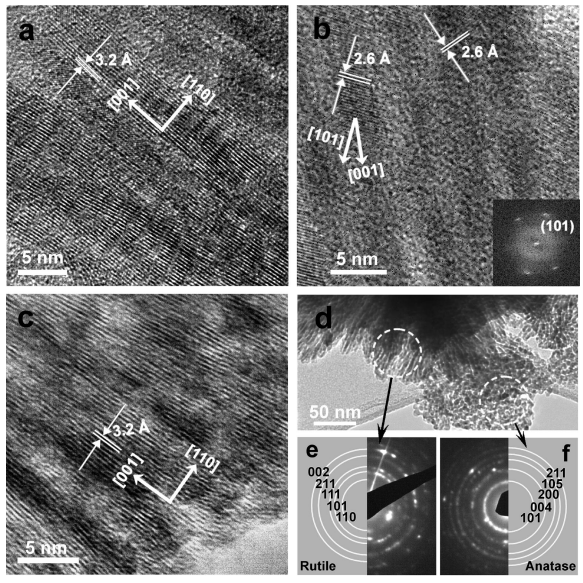

Figure 3. (a, b) High-resolution TEM images of as-synthesized MCT-12. Inset in (b) shows corresponding SAED pattern. (c) High-resolution TEM image of calcined MCT-12. (d) TEM image of aggregated spherical anatase particles outside of nanorod-based mesoporous rutile in MCT-12. (e) SAED pattern from the oriented rodlike nanocrystal area circled in (d). The diffraction ring pattern is consistent with that of rutile crystal structure. (f) SAED pattern from spherical nanoparticle area circled in (d). The diffraction ring pattern is consistent with that of anatase crystal structure.

[001]-oriented rodlike nanocrystals as building blocks in the mesoporous structure.

To further understand the role of the surfactant matrix, we studied the precipitation behavior in the solution. In a control experiment without addition of the surfactant, disordered poor crystalline anatase aggregates precipitated over time. This suggests the rutile mesostructure only forms with the surfactant mesophase. In addition, when the surfactant solution and the titanium precursor solution were mixed, the surfactant precipitated immediately with the titanium precursor, which produced a lamellar diffraction pattern (see the Supporting Information, Figure S1). However some residual, unprecipitated titanium precursor remained in the supernatant after the removal of the surfactant precipitates. Further reaction of the supernatant solution produced anatase nanoparticles at similar condition (see the Supporting Information, Figure S2). This confirms again that Ti precursor outside the surfactant mesophase produced the small amount of disordered anatase (5 wt %). Figure 3d confirms that the aggregates of spherical anatase nanoparticles were observed outside nanorod-based mesoporous rutile, as indicated by SAED patterns in images e and f in Figure 3.

From the above discussion, it is reasonable to suggest a possible mechanism (Scheme 1) for the formation of the mesostructured rutile within the surfactant mesophase similar to charge density matching mechanism observed in mesostructured silicate systems.[46] Initially, the titanium precursor cations bind with the anionic surfactant to form a lamellar mesophase. With further oxidation and condensation of TiO_2, the charge density of TiO_2 at the interface decreases due to the elimination of the positive charges in the TiO_2 framework. This promotes increase of the interfacial curvature of the surfactant matrix.[46] Thus the two-dimensional lamellar mesophase transforms into a three-dimensional mesostructure with curved interface. At the same time, crystalline rutile nanorods grow in the surfactant matrix and become fused together into the three-dimensional networks. However, the formation of the highly crystalline nanorods influences the long-range ordering and prevents the observation of high-order reflection peaks.

The exact role of the surfactant molecules in promoting the formation of the rutile phase is not yet fully understood. The different polymorphs (anatase, rutile, or brookite) can be induced by local pH variations or complexation effect.[47–49] In an aqueous solution, $TiCl_3$ hydrolyzed and oxidized to octahedral monomer ($[TiO(OH_2)_5]^{2+}$) producing acidic solution (pH 0.5).[48,50] In TiO_2, rutile crystalline structure is based on linear chains of TiO_6 octahedra by sharing equatorial edges, whereas anatase is based on a spiral chain of apical edge sharing TiO_6 octahedra.[42,47] In the interfacial region of the confined mesostructure, linear chain arrangement of $[TiO(OH_2)_5]^{2+}$ octahedral monomers (rutile nuclei) by sharing equatorial edges might be more favorable rather than apical-edge sharing spiral structures (anatase nuclei) due to the geometric confinement. The inter-rod alignment might be attributed to lattice reorientation during crystals grow, similar to an oriented attachment mechanism[51,52] commonly

(46) Monnier, A.; Schueth, F.; Huo, Q.; Kumar, D.; Margolese, D.; Maxwell, R. S.; Stucky, G. D.; Krishnamurty, M.; Petroff, P.; Firouzi, A.; Janicke, M.; Chmelka, B. F. *Science* **1993**, *261*, 1299.
(47) Zheng, Y. Q.; Shi, E. R.; Chen, Z. Z.; Li, W. J.; Hu, X. F. *J. Mater. Chem.* **2001**, *11*, 1547.
(48) Cassaignon, S.; Koelsch, M.; Jolivet, J. P. *J. Phys. Chem. Solids* **2007**, *68*, 695.
(49) Pottier, A.; Chaneac, C.; Tronc, E.; Mazerolles, L.; Jolivet, J. P. *J. Mater. Chem.* **2001**, *11*, 1116.
(50) Rotzinger, F. P.; Graetzel, M. *Inorg. Chem.* **1987**, *26*, 3704.
(51) Aizenberg, J.; Muller, D. A.; Grazul, J. L.; Hamann, D. R. *Science* **2003**, *299*, 1205.

Scheme 1. Schematic Model Illustration Showing Surfactant Templating Growth and Parallel Organization of Rodlike Rutile Nanocrystals within Surfactant Matrix

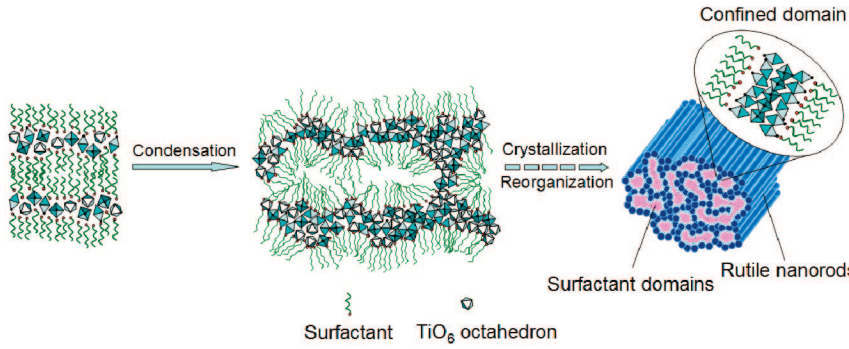

observed in solution-grown TiO_2.[52,53] During the reaction, the precursors and nuclei in the surfactant matrix should have some mobility and flexibility to relax into the low energy, crystallographically aligned configuration.[54] The rutile eventually grows into fused interconnected mesostructures within the surfactant matrix.

The highly crystalline mesoporous TiO_2 composed of oriented nanorods grown along [001] axis and with high surface area is a good candidate for Li ion insertion. It is commonly agreed that Li diffusion in rutile is highly anisotropic, which proceeds though rapid diffusion along *c*-axis [001] channels.[55] But the Li-diffusion in the ab planes is sluggish, preventing Li-ions from reaching the thermodynamically favorable octahedral sites and separating Li in the *c*-channels. Thus size reduction along the direction of ab planes in nanorod building blocks would shorten the Li diffusion distance and improve Li-insertion activities. Besides, the mesoporous structures with high surface area allow increased contact area with the electrolyte solution, enhancing electrode reactions that occur on the surfaces.

Figure 4a shows potential−capacity profiles of mesoporous crystalline TiO_2 (e.g., MCT-12) at current density of 33.6 mA/g (C/5) in the initial three charge–discharge cycles at 1–3.0 V versus Li^+/Li. The result shows that MCT-12 was able to accommodate Li up to $Li_{0.7}TiO_2$ during the first discharge and $Li_{0.63}TiO_2$ during the second discharge. Subsequently, 0.55 mol of Li per mol TiO_2 ($Li_{0.55}TiO_2$,185 mA h g^{-1}) was able to be cycled reversibly. The irreversible loss in capacity during the first charge and discharge was also observed for other TiO_2 polymorphs and nanosized rutile, which is still not clearly understood.[11–13,17–21] The sloped behavior in the potential–capacity profile is consistent with that of nanosized rutile reported previously,[11–13] which is typical of Li insertion/extraction in reversible solid solution.[12,56] Figure 4b shows potential−capacity profiles of the subsequent cycles at different charge–discharge rate. The discharge specific capacities of 210, 205, 175, and 150 mA h g^{-1} were obtained at *C*/10, *C*/5, *C*/2.5, and 1*C* rates, respectively. Derivative of the state of charge (dQ/dV) as a function of voltage is plotted in Figure 4c to identify the presence of a plateau in the first 15 cycles. Consistent with observation of a prominent plateau at potentials of 1.75 and 1.9 V in panels a and b in Figure 4, the dQ/dV vs potential profile also shows a redox reaction at 1.75 V (Li^+/Li) during discharge and 1.9 V (Li^+/Li) during charge, which appears to correspond to the $Ti^{4+/3+}$ redox reaction in the anatase phase[8,57] that existed as a minority phase in the mesoporous structure as shown in Figure 1b (note that the peak height is not indicative of the amount of materials in the differential potential profile). A prominent reduction peak at 1.4 V is also observed in the first discharge curve and weakened rapidly during cycling, which can be attributed to the irreversible formation of $LiTiO_2$ phase from rutile phase.[11,10] During cycling, redox peaks centered at 1.8 V are gradually observed, which is consistent with Li electrochemical signature of $LiTiO_2$ structure.[12,58] Figure 4d shows that the mesoporous crystalline TiO_2 was able to reversibly accommodate Li with excellent capacity retention (specific capacity of 140 mA h g^{-1}) over 100 cycles at a higher charge–discharge rate of 160 mA/g (~1*C* rate). The initial increase in specific capacity during consecutive cycling was likely due to improved wetting and contact between of electrode materials and the electrolyte, thereby giving more equilibrated performance. After the first several cycles, excellent capacity retention during Li ion insertion/extraction was observed.

Powder X-ray diffraction (XRD) technique has been used to identify the crystalline structure of the mesoporous TiO_2 after cycling of Li insertion. The Li-ion inserted mesoporous TiO_2 electrodes were removed from the cycled cells for ex-situ XRD measurement after 100 cycles. Figure 5 shows XRD patterns of two mesoporous TiO_2 electrodes after 100 cycles in fully lithiated state (discharged to 1V) and delithiated state (charged to 3V), respectively. The XRD patterns show broad reflection peaks because of nanocrystalline domains within mesoporous crystalline TiO_2. It is interesting to observe that the diffraction peaks from the initial rutile phase completely disappeared (see Figure 1b), even though the diffractions from the initial anatase phase remained. A set of new diffractions at 2θ of 43.8 and 63.5 were observed. There is no distinct difference in XRD pattern between lithiated and delithiated states in the cycled mesoporous TiO_2 electrodes. The broadness of the new reflection peaks, most likely from a Li_xTiO_2 titanate phase, is an indication of the relatively disordered nature of the new phase

(52) Banfield, J. F.; Welch, S. A.; Zhang, H. Z.; Ebert, T. T.; Penn, R. L. *Science* **2000**, *289*, 751.
(53) Penn, R. L.; Banfield, J. F. *Am. Mineral.* **1998**, *83*, 1077.
(54) Brezesinski, T.; Groenewolt, M.; Pinna, N.; Amenitsch, H.; Antonietti, M.; Smarsly, B. M. *Adv. Mater.* **2006**, *18*, 1827.
(55) Koudriachova, M. V.; Harrison, N. M.; de Leeuw, S. W. *Phys. Rev. Lett.* **2001**, *86*, 1275.
(56) Delmas, C.; Cognacauradou, H.; Cocciantelli, J. M.; Menetrier, M.; Doumerc, J. P. *Solid State Ionics* **1994**, *69*, 257.
(57) Kavan, L.; Graetzel, M.; Gilbert, S. E.; Klemenz, C.; Scheel, H. J. *J. Am. Chem. Soc.* **1996**, *118*, 6716.

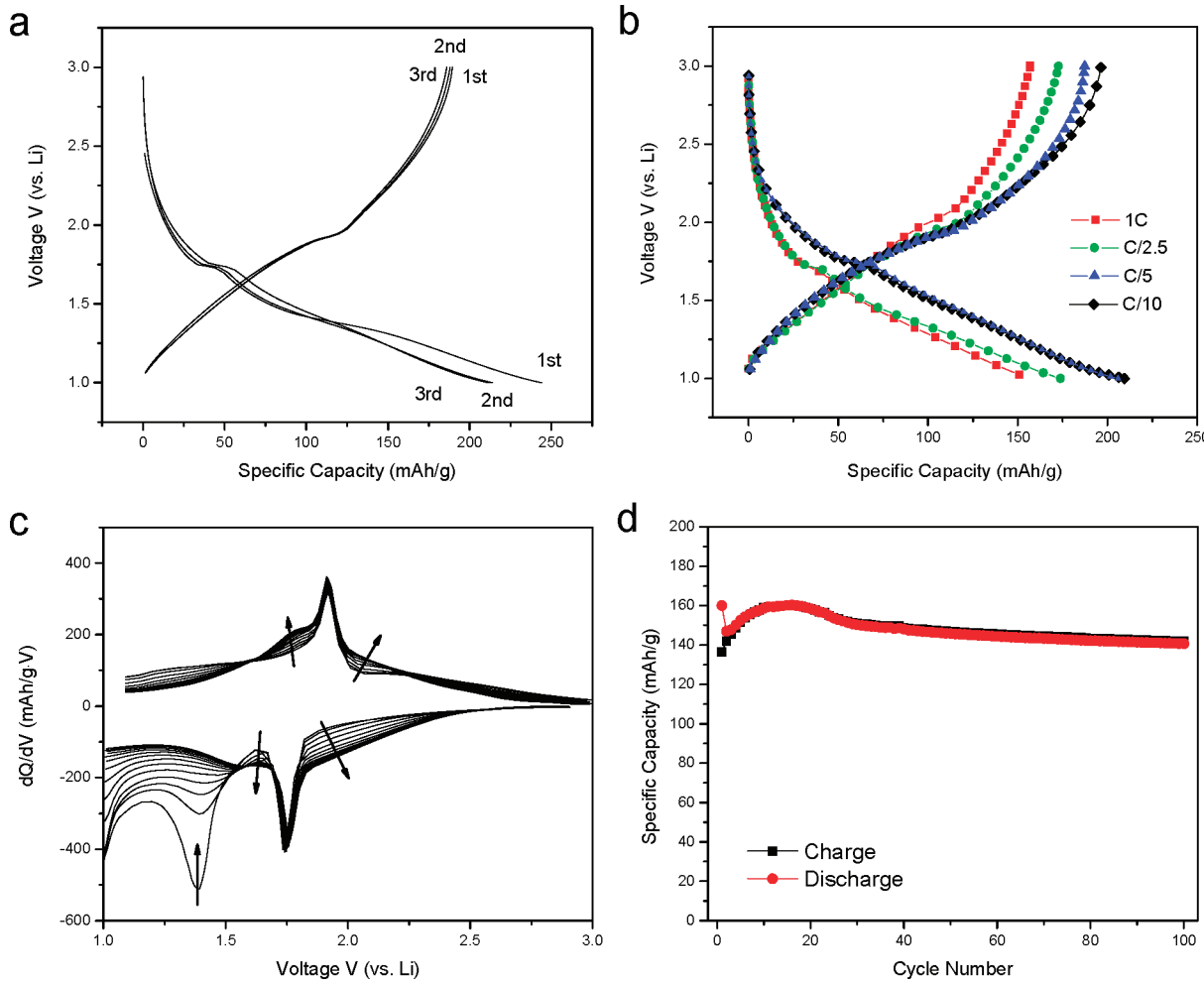

Figure 4. (a) First three potential−capacity profiles of mesoporous crystalline TiO_2 (MCT-12) at a rate of *C*/5 between voltage limits of 1 and 3 V vs Li^+/Li. (b) Fifth cycle discharge–charge capacity profile of the mesoporous crystalline TiO_2 (MCT-12) at the various rate (1*C* ∼ *C*/10) between voltage limits of 1 and 3 V. (c) d*Q*/d*V* vs potential plot of lithiated/delithiated mesoporous crystalline TiO_2. (d) Cycling behavior of mesoporous crystalline TiO_2 (MCT-12) up to 100 cycles at a 1*C* rate.

and is consistent with observations from other groups.[11,12] Hu et al. studied the XRD patterns after the first few cycles and observed a mixed pattern of $LiTiO_2$ titanate and rutile.[11] The titanate phase was attributed to the hexagonal $LiTiO_2$ phase (JCPDS 40-1053, $a = 2.881$ Å and $c = 14.602$ Å). Baudrin found out that the diffraction patterns are featureless after cycling and the new phase could not be identified.[12] They prepared an ex situ sample by mechanically grinding TiO_2 powders with lithium powder and found that the cubic rocksalt $LiTiO_2$ (JCPDS 16–0223, $a = 4.14$ Å) was formed during mechanical grinding. However, a careful study of the diffraction patterns of the cubic and hexagonal $LiTiO_2$ phase suggests that the main XRD diffractions peaks for the cubic and hexagonal phase overlap and can not be uniquely differentiated. This problem needs to be resolved by careful electron microscopy analysis. First, it is remarkable that the mesostructures in both lithiated and delithiated samples are maintained even after cycling for a long time, as shown in bright-field TEM images a and d of Figure 6, respectively. The corresponding dark-field TEM images in both lithiated (Figure 6b) and delithiated (Figure 6e) sample show that the mesoporous structure is still composed of crystalline nanorod building blocks. However, the crystalline phase of the nanorod building blocks was no longer rutile phase. The calculated *d*-spacing from three polycrystalline ring patterns in a SAED pattern (Figure 6c) are 0.204, 0.146, and 0.119 nm. To help identify the right phase, SAED patterns (Figure 6g) were taken on a cycled grain composed of oriented nanorod building blocks (Figure 6f) in a delithiated sample. Here, a set of bright spots showing a 4-fold symmetry was observed. Such 4-fold symmetry was observed in many regions. The *d*-spacing and the position of these diffraction spots enable us to conclude that the diffraction pattern is from the cubic rocksalt phase (along [001] zone axis) (JCPDS 16–0223), rather than from the hexagonal $LiTiO_2$ phase, with the specific indices as indicated in Figure 6g. Subsequently, the main diffraction rings in Figure 6c are assigned to the (200), (220), and (222) reflections of the cubic phase, and the two reflection peaks at 2θ of 43.8 and 63.5 in Figure 5 are also assigned to the (200) and (220) reflections of the cubic $LiTiO_2$ phase. Phase transformation from tetragonal rutile to cubic rocksalt $LiTiO_2$ involves rearrangement of TiO_6 octahedrons and Li insertion, which may result in morphology change. In the mesoporous TiO_2, we found that nanorod morphology and crystallographic

(58) Kavan, L.; Kalbac, M.; Zukalova, M.; Exnar, I.; Lorenzen, V.; Nesper, R.; Gratzel, M. *Chem. Mater.* **2004**, *16*, 477.

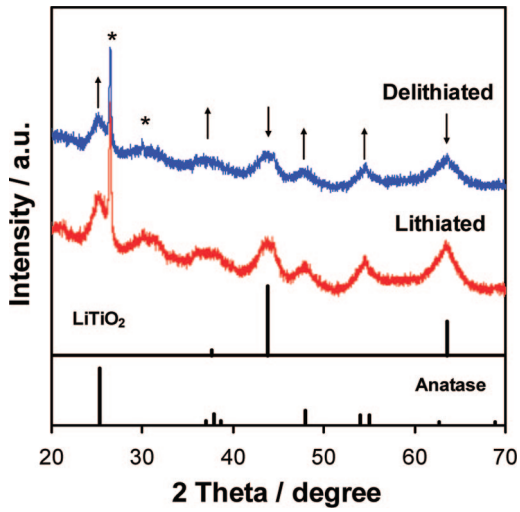

Figure 5. XRD pattern of the mesoporous TiO_2 electrodes after 100 cycles at different lithiated/delithiated state including lithiated (discharged to 1 V) and delithiated (charged to 3 V) sample. Standard reflection peaks of cubic rocksalt $LiTiO_2$ (JCPDS 16-0223) and anatase (JCPDS 21-1272) were shown as vertical bars. The diffraction lines of anatase and cubic rocksalt $LiTiO_2$ are marked by upward-directing arrows and by downward-directing arrows, respectively. Diffraction from electrode binders are marked as stars.

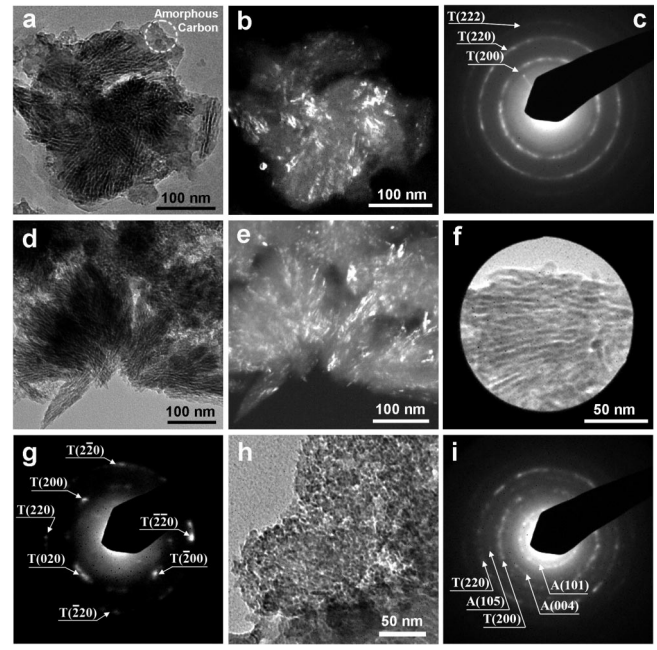

Figure 6. (a) Bright-field and (b) dark-field TEM images and (c) SAED pattern of lithiated MCT-12 after 100 cycles. Amorphous carbon is circled in (a). (200), (220), and (222) diffraction rings of cubic rocksalt $LiTiO_2$ are marked as T(200), T(220), and T(222) in (c). (d) Bright-field and (e) dark-field TEM images of delithiated MCT-12 after 100 cycles. (f) Selected area bright-field TEM image of delithiated MCT-12 composed of oriented nanorod building blocks. (g) SAED pattern of the delithiated MCT-12 in (f). (200) and (220) diffraction spots along [001] zone axis of cubic rocksalt $LiTiO_2$ are marked. (h) Bright-field TEM image of spherical particle domains in lithiated MCTs outside nanorod mesostructures. (i) SAED pattern of lithiated MCT-12 in (g) showing coexistence of anatase and cubic rocksalt $LiTiO_2$ phase. Anatase diffraction peaks (101), (004), and (105) are marked as A(101), A(004), and A(105).

alignment are maintained over electrochemical lithiation at room temperature, which may contribute to stable mesoporous structure after prolonged Li insertion/extraction cycles. In addition, the SAED pattern on the region of aggregated spherical particles (Figure 6h) outside the cubic rocksalt $LiTiO_2$ nanorod matrix confirmed the existence of anatase along with cubic rocksalt $LiTiO_2$, as indexed in Figure 6i. The anatase phase in cycled mesoporous TiO_2 electrodes is a minority phase and is very difficult to find during TEM observation. Such anatase came from initial small portion of aggregated spherical anatase particle (Figure 3d). An amorphous carbon layer in the electrode materials can be observed around mesoporous particles, as shown in a circled region in Figure 6a. During TEM investigation, we have not identified formation of significant amount of amorphous TiO_2, although we will not exclude formation of amorphous TiO_2 on the particle surface during Li insertion/extraction. The process of the amorphous TiO_2 formation and its role on electrochemical properties are still a subject for further investigation.

Conclusions

In summary, we developed a low-temperature approach to produce highly crystalline mesoporous rutile TiO_2 that are comprised mainly of interconnected rutile nanorods aligned along [001] direction. The crystalline rutile mesostructures formed only within the surfactant mesophase and with a stable high surface areas and narrow pore size distributions. The pore size was dependent on the surfactant chain length and thus tunable. The mesoporous rutile TiO_2 demonstrates excellent Li-insertion activity, which can accommodate up to $Li_{0.7}TiO_2$ during the first discharge. Up to 0.55 Li ($Li_{0.55}TiO_2$, 185 mA h g^{-1}) can be charged and discharged reversibly at C/5 rate in the subsequent cycles with excellent capacity retention. Rutile nanorod building blocks are irreversibly transformed into cubic rocksalt $LiTiO_2$ nanorods and mesoporous structures remain stable over Li ion insertion cycles. More recently we found that the properties of such materials (high rate performance) can be further improved through increasing nanorod crystallinity or incorporating conductors into the mesostructures. Controlled nanostructures therefore provide a good opportunity to understand and optimize the structure–property relationships. Furthermore, the crystalline mesoporous rutile may also have good potential for other applications such as stable catalyst supports.

Acknowledgment. This work is supported by the Laboratory-Directed Research and Development Program (LDRD) of the Pacific Northwest National Laboratory (PNNL) and by the Office of Basic Energy Sciences (BES), U.S. Department of Energy (DOE). The TEM work was carried out at the Environmental and Molecular Science Laboratory, a national scientific user facility sponsored by the DOE's Office of Biological and Environmental Research (BER). PNNL is a multiprogram laboratory operated by Battelle Memorial Institute for the Department of Energy under Contract DE-AC05-76RL01830. Sandia National Laboratory is a multiprogram laboratory operated by Sandia Corporation, a Lockheed Martin Company, for the United States Department of Energy's National Nuclear Security Administration under Contract DEAC04-94AL85000.

Supporting Information Available: XRD of Ti precursor/surfactant mesostructure and TEM image of anatase phase (PDF). This information is available free of charge via the Internet at http://pubs.acs.org.

CM8002589